

Article

Understanding of Active Sites and Interconversion of Pd and PdO during CH₄ Oxidation

Dong Gun Oh ^{1,†}, Hristiyan A. Aleksandrov ^{2,*,†}, Haneul Kim ¹, Iskra Z. Koleva ²,
Konstantin Khivantsev ^{3,*}, Georgi N. Vayssilov ² and Ja Hun Kwak ^{1,*}

¹ School of Energy and Chemical Engineering, Ulsan National Institute of Science and Technology (UNIST), 50 UNIST-gil, Ulsan 44919, Republic of Korea

² Faculty of Chemistry and Pharmacy, University of Sofia, 1126 Sofia, Bulgaria

³ Institute for Integrated Catalysis, Pacific Northwest National Laboratory, Richland, WA 99352, USA

* Correspondence: haa@chem.uni-sofia.bg (H.A.A.); konstantin.khivantsev@pnnl.gov (K.K.);

jhkwak@unist.ac.kr (J.H.K.)

† These authors contributed equally to this work.

Abstract: Pd-based catalysts are widely used in the oxidation of CH₄ and have a significant impact on global warming. However, understanding their active sites remains controversial, because interconversion between Pd and PdO occurs consecutively during the reaction. Understanding the intrinsic active sites under reaction conditions is critical for developing highly active and selective catalysts. In this study, we demonstrated that partially oxidized palladium (PdO_x) on the surface plays an important role for CH₄ oxidation. Regardless of whether the initial state of Pd corresponds to oxides or metallic clusters, the topmost surface is PdO_x, which is formed during CH₄ oxidation. A quantitative analysis using CO titration, diffuse reflectance infrared Fourier-transform spectroscopy, X-ray diffraction, and scanning transmission electron microscopy demonstrated that a surface PdO layer was formed on top of the metallic Pd clusters during the CH₄ oxidation reaction. Furthermore, the time-on-stream test of CH₄ oxidation revealed that the presence of the PdO layer on top of the metallic Pd clusters improves the catalytic activity. Our periodic density functional theory (DFT) calculations with a PdO_x slab and nanoparticle models aided the elucidation of the structure of the experimental PdO particles, as well as the experimental C-O bands. The DFT results also revealed the formation of a PdO layer on the metallic Pd clusters. This study helps achieve a fundamental understanding of the active sites of Pd and PdO for CH₄ oxidation and provides insights into the development of active and durable Pd-based catalysts through molecular-level design.

Keywords: active site; CH₄ oxidation; DRIFTS; PdO_x



Citation: Oh, D.G.; Aleksandrov, H.A.; Kim, H.; Koleva, I.Z.; Khivantsev, K.; Vayssilov, G.N.; Kwak, J.H. Understanding of Active Sites and Interconversion of Pd and PdO during CH₄ Oxidation. *Molecules* **2023**, *28*, 1957. <https://doi.org/10.3390/molecules28041957>

Academic Editors: Ioannis V. Yentekakis and Alessandra Puglisi

Received: 29 December 2022

Revised: 2 February 2023

Accepted: 15 February 2023

Published: 18 February 2023



Copyright: © 2023 by the authors. Licensee MDPI, Basel, Switzerland. This article is an open access article distributed under the terms and conditions of the Creative Commons Attribution (CC BY) license (<https://creativecommons.org/licenses/by/4.0/>).

1. Introduction

Natural gas, mainly consisting of methane, has received considerable attention as an alternative fuel for automobiles owing to its high energy efficiency. Furthermore, it is environmentally friendly, because it generates fewer undesirable by-products per unit energy when compared with other fossil fuels, such as gasoline and diesel. However, unburned CH₄ contributes significantly to global warming due to its ~20 times higher greenhouse potential than that of carbon dioxide. Therefore, significant research efforts have been dedicated to eliminating CH₄ from exhaust gas.

Pd-supported catalysts are the most widely used catalysts for methane oxidation because of their high catalytic activity [1–8]. Despite significant research on catalytic active sites over the past decade, the understanding of the nature of the active sites on Pd-supported catalysts remains limited. Müller et al. proved the role of lattice oxygen on PdO nanoparticles (NPs) using labeled ¹⁸O, suggesting that CH₄ oxidation follows the Mars-van Krevelen mechanism [9]. Iglesia et al. reported that the CH₄ oxidation reaction occurs via the redox cycle of the PdO surface [10,11]. Jang et al. demonstrated that

the PdO_x species generated under the reaction conditions exhibited a linear correlation with CH₄ oxidation activity on Pd and Pt–Pd bimetallic catalysts [12]. On the contrary, Lyubovsky et al. suggested that metallic Pd is more active toward methane oxidation than PdO at high temperatures [13]. Xu et al. also proposed that CH₄ oxidation occurs on the metallic Pd surface via the Langmuir–Hinshelwood mechanism, and the stability of metallic Pd is important for CH₄ oxidation activity at low temperatures [14]. Hellman et al. reported that CH₄ easily dissociates from the partially reduced PdO(101) or metallic Pd rather than from PdO(100), using density function theory (DFT) calculations [15]. Furthermore, Zorn et al. reported that fully oxidized PdO did not participate in the reaction [16], and Mehar et al. reported that an intrinsic active site for Pd-based catalysts is not single-layer PdO(101) but multilayer PdO(101) [17].

Despite numerous studies on the active sites for CH₄ oxidation, the understanding of their nature remains limited. In this study, we investigated the behavior of Pd and PdO under the reaction conditions to establish the active sites for CH₄ oxidation. An investigation using CO titration, diffuse reflectance infrared Fourier-transform spectroscopy (DRIFTS), and in situ X-ray diffraction (XRD) revealed that the initially formed PdO does not change during the CH₄ oxidation reaction. However, when it started from the metallic Pd cluster, a surface PdO layer gradually formed on the metallic Pd core during CH₄ oxidation. Notably, regardless of whether the initial state of Pd corresponds to oxides or metallic clusters, the topmost surface is PdO_x, suggesting that it is most probably the active site, and it is crucial for the activity and durability of CH₄ oxidation. To understand the structure of the experimental PdO particles, we identified the most stable positions for the O species on the surface and subsurface regions of the Pd(111) slab models at different coverages. In addition, we also interpreted the DRIFTS results of CO on PdO by employing Pd₇₉ nanoparticle models in our periodic density functional theory (DFT) calculations. This study helps to achieve a fundamental understanding of the active sites for CH₄ oxidation and provides insights into the development of active and durable Pd-based catalysts through molecular-level designs.

2. Results and Discussion

2.1. Characterization of Pd/Al₂O₃ Catalysts

To understand the behavior of Pd and PdO under reaction conditions for CH₄ oxidation, we prepared 5.5 wt% Pd/Al₂O₃ via hydrothermal aging (HTA) at 850 °C and characterized them using XRD and STEM after oxidative and reductive pretreatments at 500 °C, as shown in Figures 1 and 2. The oxidative pretreatment is denoted as “O_x”, and the reductive pretreatment is denoted as “Red”. The XRD patterns display the phase transformation of the support from γ -Al₂O₃ (Figure 1a) to δ -Al₂O₃ (Figure 1b) during the HTA. Pd/Al₂O₃-O_x and Pd/Al₂O₃-Red in Figure 1c,d exhibit characteristic peaks attributed to PdO at $2\theta = 29.3^\circ, 33.9^\circ, \text{ and } 41.9^\circ$ and $2\theta = \text{Pd at } 40^\circ$, respectively. The crystallite sizes of PdO and Pd estimated using the Scherrer equation are 15 nm and 30 nm, respectively. In contrast, the STEM images and particle size distribution displayed in Figure 2 clearly show significantly large PdO and Pd clusters of size 70 nm for oxidation and 53 nm for reduction. Datye et al. proposed that large metallic Pd clusters form polycrystalline metastable Pd/PdO structures during phase transformation [18,19]. Therefore, it can be interpreted that some of palladium during HTA is auto-reduced [20,21] and forms a polycrystalline Pd/PdO structure, which is consistent with the residual metallic Pd clusters shown in Figure 1c. The size discrepancy between the XRD and TEM results also elucidates that the Pd/PdO structure is polycrystalline with several grain boundaries, as shown in Supplementary Materials Figure S1. Based on the XRD and TEM results, the significant size discrepancy between PdO and Pd is caused by the polycrystalline nature of the Pd/PdO structure.

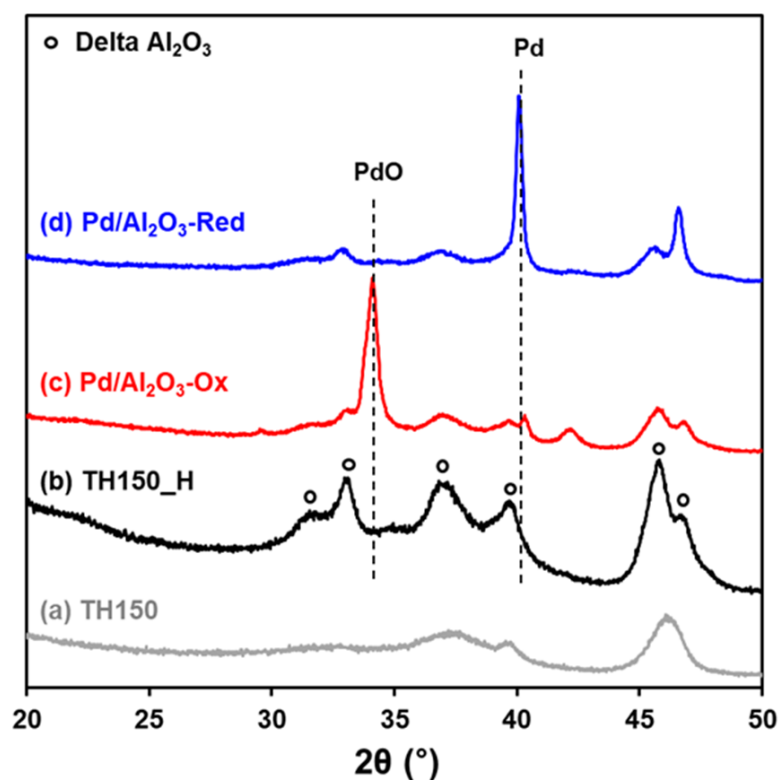


Figure 1. XRD patterns of bare TH150 (a) before and (b) after HTA, and 5.5 wt% Pd/Al₂O₃ with (c) oxidative and (d) reductive pretreatment.

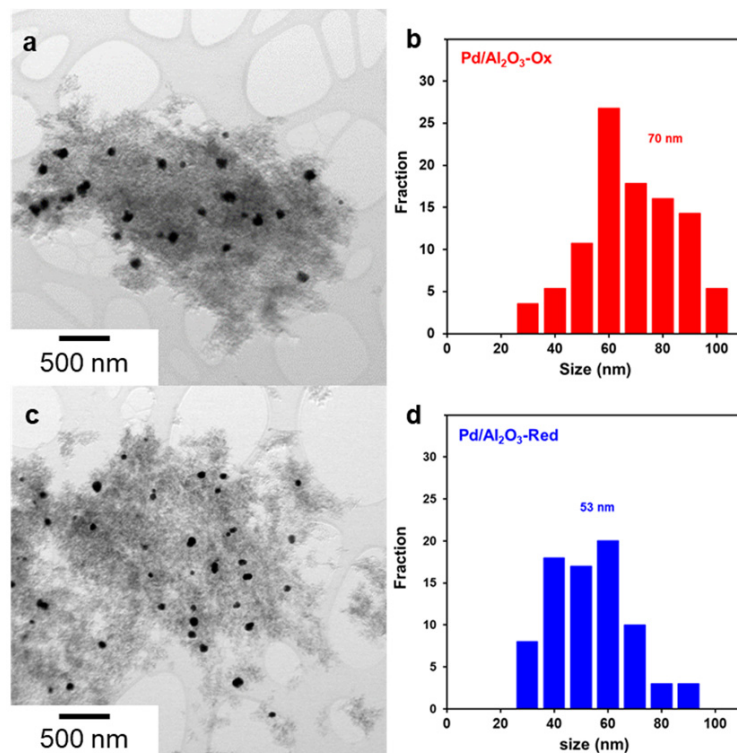


Figure 2. TEM images of (a) Pd/Al₂O₃-O_x and (c) Pd/Al₂O₃-Red, and particle size distribution of (b) Pd/Al₂O₃-O_x and (d) Pd/Al₂O₃-Red.

2.2. Catalytic Behaviors of Pd/Al₂O₃ Catalysts

To investigate the difference in effects of oxidative and reductive pretreatments on catalytic behavior, we performed the CH₄ oxidation reaction at 340 °C for 8 h, as shown in Figure 3. Significantly, the initial activity was comparable regardless of whether it was the oxidative or reductive pretreatment. Accordingly, it can be inferred that the active sites of Pd/Al₂O₃-O_x and Pd/Al₂O₃-Red are most likely to be similar under the reaction conditions. Notably, the decrease in the catalytic activity of Pd/Al₂O₃-Red was slower than that of Pd/Al₂O₃-O_x over 8 h of CH₄ oxidation. This indicates that the reductive pretreatment of Pd/Al₂O₃ catalysts can improve their durability for CH₄ oxidation compared to oxidative pretreatment. To understand the reason for this observation, we characterized the bulk and surface properties under the reaction conditions through CO titration, in situ XRD, DRIFTS, and STEM.

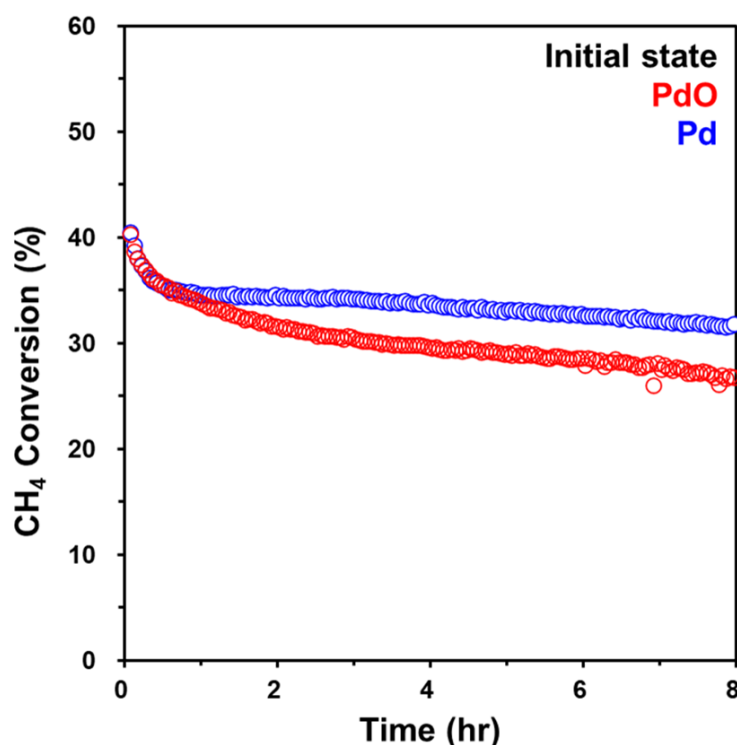


Figure 3. Conversion of CH₄ oxidation as a function of time for Pd/Al₂O₃-O_x (red) and Pd/Al₂O₃-Red (blue). Reaction conditions: 1% CH₄; 10% O₂ in He at 340 °C.

We should point out that, in the oxidized sample, the catalytic activity decreases from 40% to around 28% after 8 h of reaction. The issue with the deactivation of the Pd catalyst in the investigation reaction is complex and generally agreed to be related to the presence of water vapor [22–31], which forms during methane oxidation. Water competes with methane for the active sites on the catalyst surface, since it can dissociate and block the catalytically active undercoordinated Pd sites, forming a spectator Pd-OH species; the effective removal of strongly adsorbed OH species from the PdO surface occurs only at temperatures in excess of 500 °C [31,32].

2.3. Comparison of Pd and PdO under the Reaction Conditions

To investigate the transformation of metallic Pd and PdO during the reaction, we used CO titration after the reaction had progressed for a certain period of time to quantify the oxygen to ascertain the relative proportion of PdO in the Pd/PdO cluster, as shown in Figure 4. The reaction conditions for CH₄ oxidation are the same as those described above, and CO titration was also performed at the same temperature after sufficiently purging with He. The initial analysis of Pd/Al₂O₃-O_x showed 100% of PdO, and it did not change

during the course of the reaction over a period of 8 h. Therefore, there is no change in PdO during the CH₄ oxidation reaction. However, interestingly, for Pd/Al₂O₃-Red, the PdO contents gradually increased as the reaction progressed and plateaued at ~44% of PdO after 3 h of reaction, which is consistent with the previous observations that metallic Pd is oxidized during the reaction [14]. Moreover, during CH₄ oxidation at 340 °C, small-sized Pd clusters (<3 nm) completely oxidize to PdO (Figure 5). Based on these results, we inferred that metallic Pd is oxidized under the reaction conditions, forming a PdO layer on top of the metallic Pd clusters. The thickness of the PdO phase is ~1.3–1.5 nm. Thus, in the case of smaller crystallites whose size is not sufficient to form the surface PdO layer on metallic Pd clusters, Pd is fully oxidized to PdO.

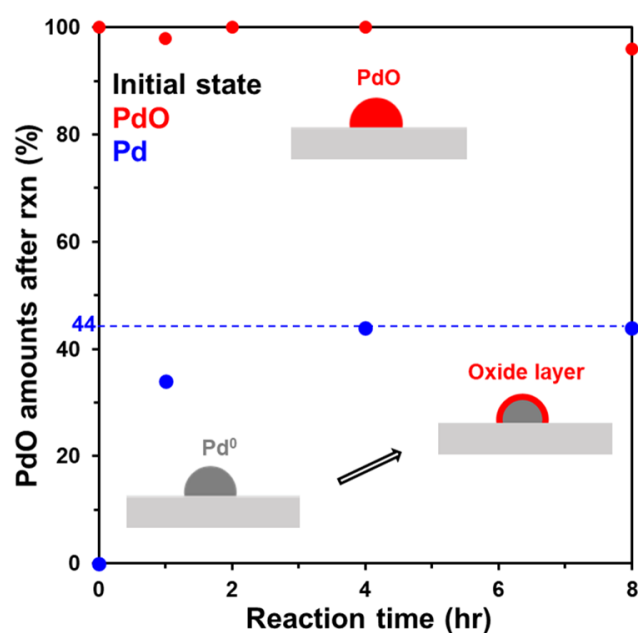


Figure 4. PdO quantity estimated via CO titration as a function of time. Reaction conditions: 1% CH₄; 10% O₂ in He at 340 °C; CO titration: 10% CO/He in 1 mL loop at 340 °C.

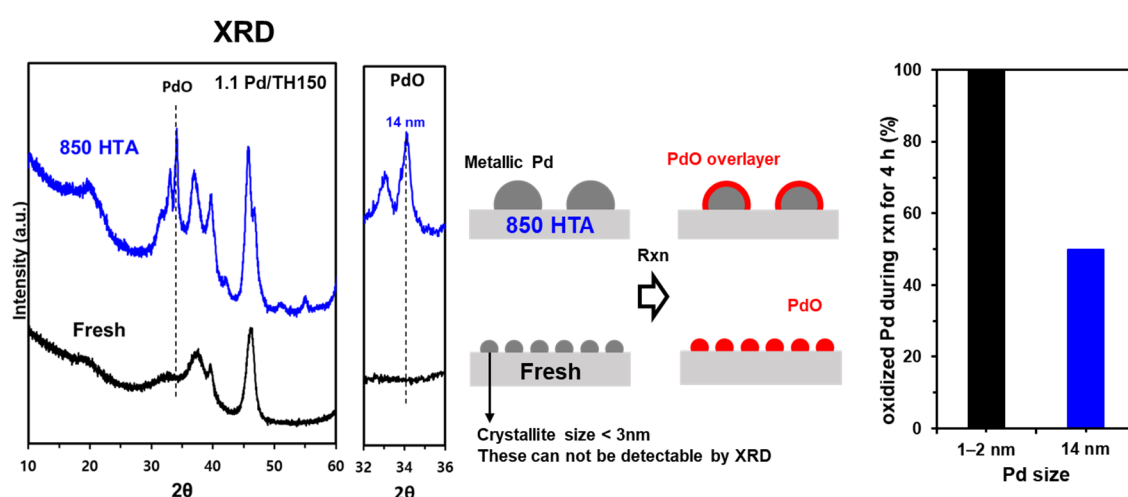


Figure 5. XRD patterns for 1.1 wt% Pd/Al₂O₃ before (black) and after HTA (blue) (left), scheme for redox behavior of Pd clusters (middle), and oxidized Pd during the CH₄ oxidation of 4 h estimated by CO titration (right). As shown in XRD, Pd species were not detected because of their small size (<3 nm) on fresh 1.1 wt% Pd/Al₂O₃ catalysts. These small Pd species were fully re-oxidized to PdO during the CH₄ oxidation of 4 h. Reaction conditions: 1% CH₄; 10% O₂ in He at 340 °C.

To confirm this inference, we performed in situ XRD experiments with different pretreatments under the reaction conditions (Figure 6). Both catalysts exhibit common peaks, which are attributed to δ - Al_2O_3 . XRD patterns for Pd/ Al_2O_3 -Red demonstrate only metallic Pd at $2\theta = 40^\circ$, but Pd/ Al_2O_3 - O_x shows PdO at $2\theta = 33.9^\circ$ with a little metallic Pd at $2\theta = 40^\circ$, as mentioned above (Figure 6a). After the reaction, the XRD patterns of Pd/ Al_2O_3 - O_x did not change, which indicates that PdO does not change during the reaction, which is in agreement with the CO titration results. In contrast, for Pd/ Al_2O_3 -Red, a broad PdO phase was formed, and simultaneously, a slight decrease in the metallic Pd content was observed during the reaction (Figure 6b). Based on the CO titration results, the broad PdO phase is attributed to the $\sim 44\%$ of PdO generated during the reaction.

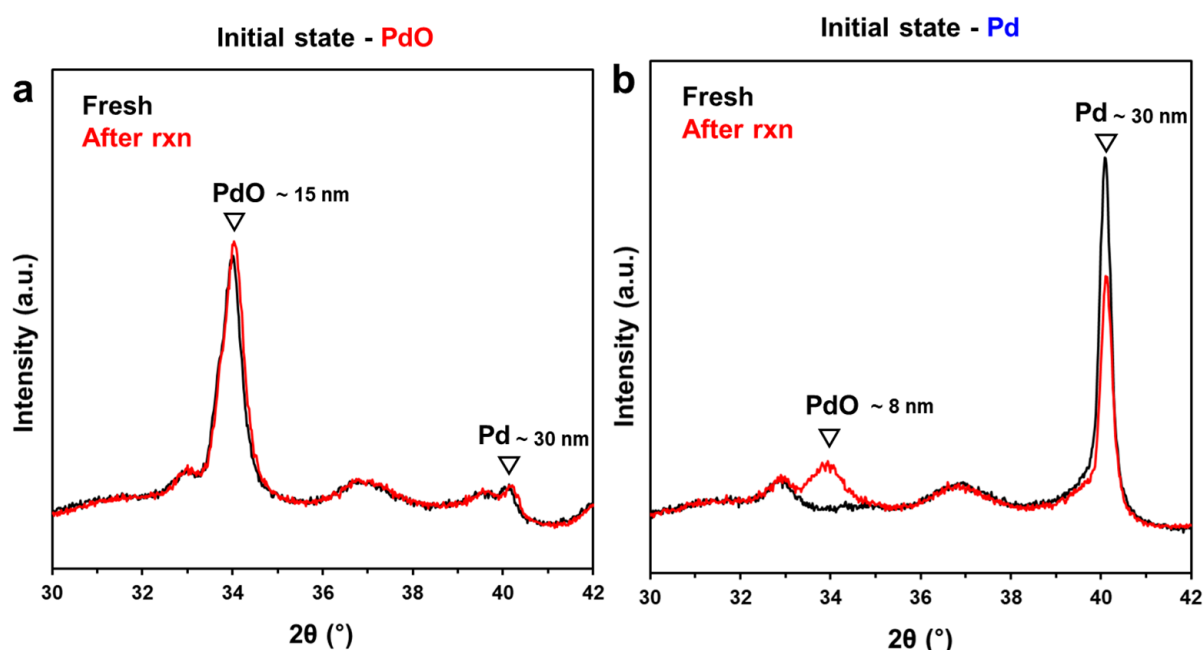


Figure 6. In situ XRD patterns of (a) Pd/ Al_2O_3 - O_x and (b) Pd/ Al_2O_3 -Red before (black) and after (red) 8 h of CO oxidation.

Furthermore, to confirm the generation of the surface PdO layer, we characterized the surface compositions using DRIFTS after CO adsorption, as shown in Figure 7. The catalysts were tested over a period of 8 h of CH_4 oxidation under the same conditions in DRIFTS cells, and subsequently, IR spectra were collected after CO adsorption at RT following He purging. The IR spectrum of Pd/ Al_2O_3 - O_x obtained before the reaction shows a representative band of PdO $_x$ at 2140 cm^{-1} [12] and a broad band at $2100\text{--}2090\text{ cm}^{-1}$ attributed to metallic Pd, which was partially reduced during CO adsorption [16]. The IR spectrum of Pd/ Al_2O_3 -Red collected before the reaction shows a distinctive peak at 2080 cm^{-1} , which is attributed to linear-bound CO, and two peaks at 1980 and 1940 cm^{-1} , which are attributed to bridge-bound CO on metallic Pd. The IR spectrum of Pd/ Al_2O_3 - O_x obtained after 8 h of reaction (Figure 7a) shows a similar profile to that before the reaction, indicating that the initially formed PdO does not change during the reaction, which is in good agreement with the above results. However, on Pd/ Al_2O_3 -Red, partially oxidized PdO $_x$ at 2140 cm^{-1} appeared with the disappearance of bridge-bound CO on metallic Pd, yielding a similar spectrum to that of Pd/ Al_2O_3 - O_x . Notably, regardless of whether the initial state was metallic Pd or PdO, the catalysts showed the same topmost surface after the reaction.

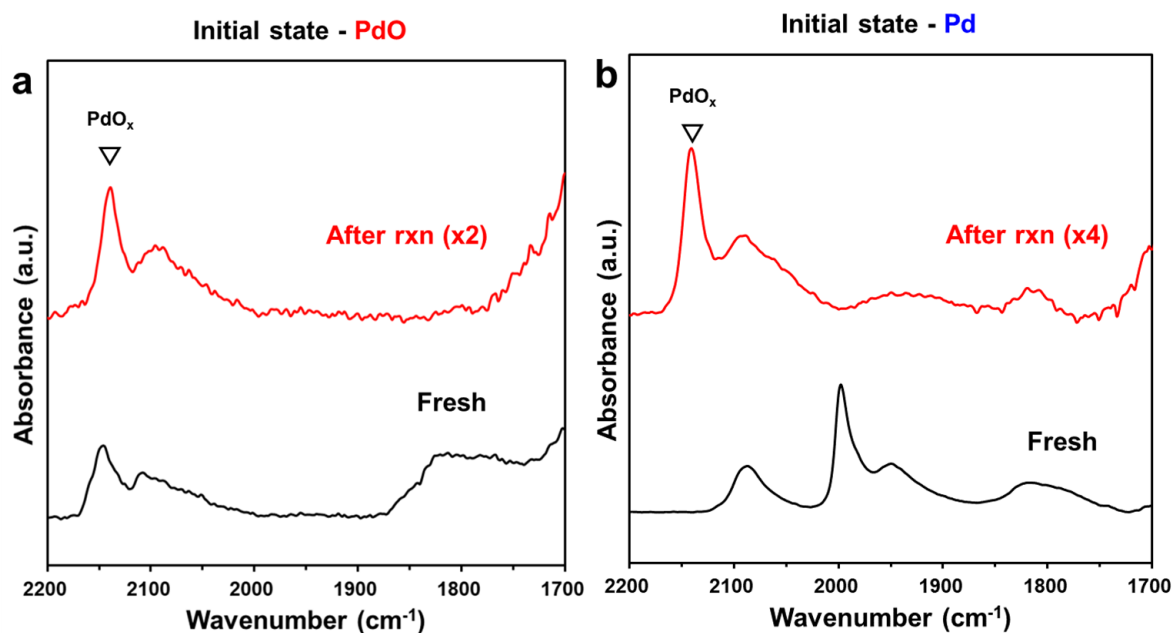


Figure 7. In situ DRIFTS spectra of adsorbed CO on (a) Pd/Al₂O₃-Ox and (b) Pd/Al₂O₃-Red before (black) and after (red) 8 h of CO oxidation. DRIFTS spectra were recorded at 25 °C after He purging.

In addition, as shown in Figure S2, the surface transformation from Pd to PdO occurred within 3 min of the reaction. Based on these results, we interpreted that the immediately generated topmost PdO_x during the reaction is the active site for CH₄ oxidation, and the similarity in the initial activity of Pd/Al₂O₃-Ox and Pd/Al₂O₃-Red in Figure 3 is due to the presence of the same active site—the topmost PdO_x surface. STEM on Pd/Al₂O₃-Red after 8 h of reaction also demonstrated the formation of a PdO surface layer, as shown in Figure 8. The high magnification image of Pd/Al₂O₃-Red-Rxn 8 h reveals PdO lattice fringes of 0.308 nm and 0.258 nm, corresponding to the PdO(100) and (101) directions, respectively.

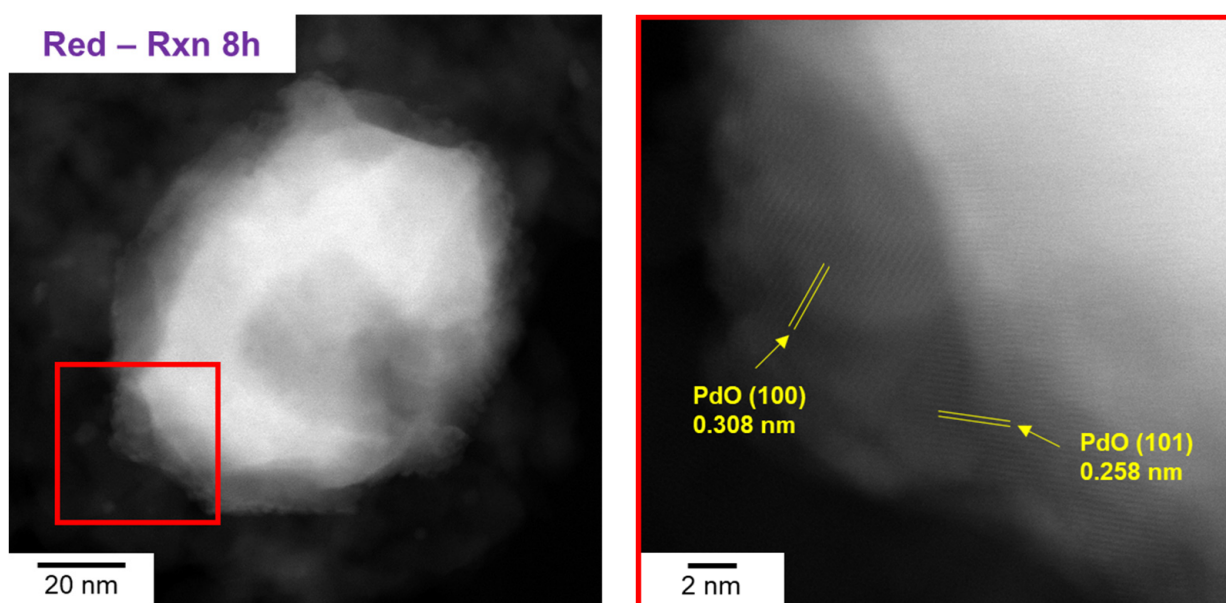


Figure 8. High-magnification STEM images of Pd/Al₂O₃-Red-Rxn (8 h).

Based on the in situ XRD, DRIFTS, and STEM results, Pd/Al₂O₃-Red after CH₄ oxidation reaction consists of a metallic Pd core with a surface PdO layer of 44%. This interpretation is consistent with the findings of Lee et al., who reported that the surface PdO layer on

the metallic Pt core enhances the activity and long-term durability of CH₄ oxidation [33]. Furthermore, it is also related to the report of Mehar et al. that multilayer PdO(101) on Pd(100) exhibited a better catalytic performance than single-layer PdO(101) [17]. Based on these results, we thought that the formation of the PdO layer on the metallic Pd core is the reason for the improved catalytic stability of Pd/Al₂O₃-Red shown in Figure 3. In Figure 6b, metallic Pd is dominant after the reaction, and someone can consider this as evidence that metallic Pd might be the active site. However, it is important to note that, regardless of whether it is the PdO or PdO/Pd core-shell structure, both catalysts have practically the same topmost active surface of PdO_x.

2.4. DFT Modeling of the Interaction of O Species with Pd(111) Surface and Pd₇₉ Nanoparticle Models

Periodic DFT calculations were employed to clarify our experimental results. First, we compared the adsorption of one O atom on all available surfaces and subsurface positions of the Pd(111) model (Figure 9). The most stable position was found to be the surface fcc, as the O species located initially at the br and oss positions also moved during the geometry optimization to fcc. The other three-fold hollow position, hcp, is less stable by 0.18 eV than the fcc position. The destabilization of the subsurface positions, tss and tss', is much higher at 1.32 and 1.95 eV, respectively, with respect to the fcc position.

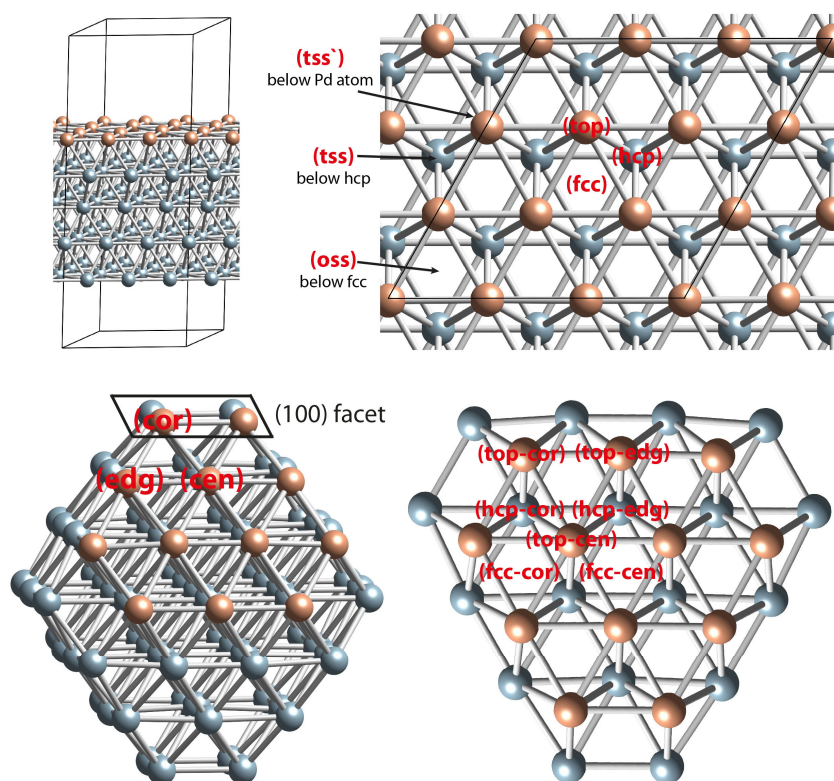


Figure 9. Notation of the site locations for the slab and NP models. Color coding: atoms from Pd top surface layer—orange; other Pd atoms—light blue.

To explore the coverage effect, we also considered models with high O surface coverage, where nine O centers are located on the available three-fold (fcc or hcp) surface sites. Similar to the situation with one O center, the model with nine O centers in fcc positions is more stable by 1.74 eV (0.19 eV per O center) than the model with nine hcp O centers. Further, we considered models with high surface and subsurface O coverage. The most stable configuration was found with nine O_{fcc} and nine O_{tss}, as it is more stable by 1.34 eV (0.07 eV per O center) than the structure with nine O centers located at the fcc and tss' positions. The structure with the initial configuration 9O_{hcp}9O_{oss} converts into the most

stable one, $9O_{fcc}9O_{tss}$, during the geometry optimization. Thus, on the surface saturated by O Pd(111) and Pd₇₉ models considered below, we positioned the surface and subsurface O species at the most stable fcc and tss positions, respectively.

Further, we also modeled the process of O migration in the Pd₇₉ nanoparticle model from the center of the (111) facet (fcc-cen position) to the subsurface region (oss-cen position) at low and high O surface coverages, where only one fcc-cen position and all fcc surface positions (62 in total) are occupied by O centers, respectively (Figure 10, Table 1). At low coverage, the process is strongly endothermic by 2.26 eV (Table 1). At the initial state (IS) structure, Pd₇₉O-IS, the three Pd-O bond lengths are 199 pm. During the subsurface migration, the O center penetrates through a Pd₃ triangle located at the center of the (111) facet. Initially, Pd-Pd distances in this triangle are 286–287 pm. In the TS structure, the O center is already located below the Pd surface layer, as the Pd-O distances with the closest Pd surface and subsurface atoms are 201–202 and 232–237 pm, respectively (Table 1). The Pd₃ triangle is slightly extended, as the corresponding Pd-Pd distances are 308–312 pm. It is shrunk back at the Pd₇₉O-FS structure, where the Pd-Pd distance, 288 pm, is similar to the corresponding values in the Pd₇₉O-IS structure. On the other hand, the positions of the penetrating O center are close at the Pd₇₉O-TS and Pd₇₉O-FS structures, as the Pd(subsurface)-O distances in the Pd₇₉O-FS structure are by ~10 pm shorter, while the Pd(surface)-O bond lengths are by ~10 longer in comparison to the corresponding distances in the Pd₇₉O-TS structure. The “late” nature of the TS is also confirmed by the calculated activation barrier, 2.28 eV, which is similar to the endothermicity of the migration process.

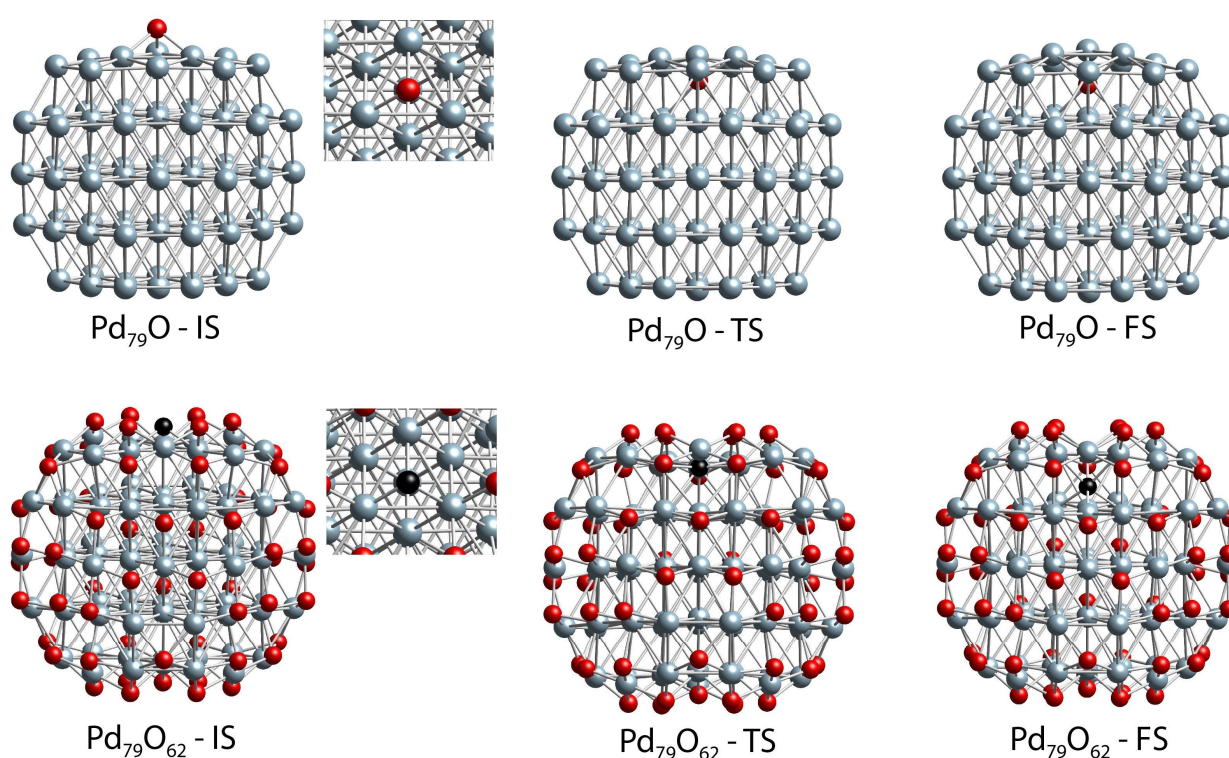


Figure 10. Side and local top (for IS structures only) views of the initial, transition, and final state structures (IS, TS, and FS) for the $O_{fcc-cen}$ subsurface diffusion to the oss-cen position in the Pd₇₉O and Pd₇₉O₆₂ models. Color coding: Pd—blue; O—red; the penetrating $O_{fcc-cen}$ atom in Pd₇₉O₆₂ models—black.

Table 1. Energy and activation barriers (in eV) of the O migration from the surface to the subsurface region at the center of the (111) facet of Pd₇₉ NP at low and high O surface coverage. Structural characteristics (Pd–O and Pd–Pd distances in pm) of the initial, transition, and final state structures are also shown.

Structure	E [‡]	ΔE	Pd–O	Pd–Pd
Pd ₇₉ O-IS	2.28	2.26	199 ^a ;199 ^a ;199 ^a	286;287;287
Pd ₇₉ O-TS			201 ^a ;202 ^a ;202 ^a /232 ^b ;233 ^b ;237 ^b	308;310;312
Pd ₇₉ O-FS			210 ^a ;210 ^a ;211 ^a /222 ^b ;223 ^b ;223 ^b	288;288;288
Pd ₇₉ O ₆₂ -IS	1.17	0.31	198 ^a ;198 ^a ;198 ^a	298;298;298
Pd ₇₉ O ₆₂ -TS			195 ^a ;196 ^a ;196 ^a	338;339;340
Pd ₇₉ O ₆₂ -FS			218 ^a ;218 ^a ;219 ^a /216 ^b ;216 ^b ;216 ^b	277;277;277

^a Pd–O distances that include surface Pd atoms; ^b Pd–O distances that include subsurface Pd atoms.

The occupation of all fcc surface positions by O atoms in the Pd₇₉O₆₂ system leads to expansion of the Pd₇₉ NP, as can be seen from the Pd–Pd distances. At the Pd₇₉O₆₂-IS structure in the Pd₃ triangle, they are longer by ~13 pm than those at the Pd₇₉O-IS structure. Simultaneously, the Pd–O bond lengths are similar at both structures. At the Pd₇₉O₆₂-TS structure, the penetrating O center is close to the plane defined by the three Pd atoms of the Pd₃ triangle. In this structure, the Pd–Pd distances are elongated by 40 pm in comparison to the corresponding values at the Pd₇₉O₆₂-IS structure, while the Pd–O distances are 2–3 pm shorter in the Pd₇₉O₆₂-TS structure. When the O center arrives in the subsurface layer, it is essentially equidistantly positioned between the surface and subsurface Pd atoms, while the Pd₃ triangle notably shrinks as the corresponding Pd–Pd are only 277 pm in the Pd₇₉O₆₂-FS. The population of all surface positions by O leads to a dramatic decrease of the endothermicity of the O penetration process from 2.26 to 0.31 eV, as the activation barrier is also reduced by almost 50%, from 2.28 to 1.17 eV (Table 1).

2.5. DFT Modeling Adsorption of CO Species on Oxidized Pd(111) and Pd Nanoparticle

In our previous work, we reported CO adsorption on different positions of pristine Pd₇₉ palladium nanoparticles. Here, we considered CO adsorption on an oxidized palladium surface and nanoparticles. For CO adsorption on the oxidized palladium surface, we used Pd(111) slab models containing O species (Figure 10) at fcc positions. Our calculations showed that, if all nine fcc positions in the unit cell are occupied by O species, the adsorption of CO is not favorable, as the molecule desorbs from the surface during the geometry optimization. The CO can adsorb on the top if at least two neighboring fcc positions are unoccupied, i.e., on the (O_{fcc})₇/Pd(111) model, though, even in this model, the BE of CO is as low as −0.17 eV. Much stronger CO adsorption can be achieved when three neighboring fcc positions are free, as the BE values are similar for CO adsorbed on the top and hcp positions, −0.99 and −0.92 eV (Table 2). We also considered CO adsorption on Pd(111) models, where O species occupy not only the surface but also all nine tss subsurface positions. Interestingly, the presence of subsurface O species strengthened the interaction of CO with the Pd(111) surface, as the BE values for the structures Pd111/(O_{fcc})₇(O_{tss})₉_CO_top, Pd111/(O_{fcc})₆(O_{tss})₉_CO_hcp, and Pd111/(O_{fcc})₆(O_{tss})₉_CO_top, −0.26, −1.02, and −1.65 eV are higher as absolute values than the corresponding values for the models that do not contain O species in the subsurface region. These results also highlight that CO prefers on-top adsorption at high O surface and subsurface coverage.

Table 2. Calculated energetic and structural characteristics of the adsorption complexes of one CO molecule on the oxidized Pd(111) slab model and palladium nanoparticles, as well as PdO(101) and Pd(100) slab models. Energy values are in eV, distances in pm, and vibrational frequencies in cm^{-1} .

Structure	BE ^a	CN ^b	r(Pd-C)	$\nu(\text{C-O})$	$\Delta r(\text{C-O})$ ^c
Oxidized palladium surface					
Pd111(O _{fcc}) ₇ /CO_top	−0.17	9	194	2085	0.5
Pd111(O _{fcc}) ₆ /CO_hcp	−0.92	9;9;9	211;211;211	1873	3.4
Pd111(O _{fcc}) ₆ /CO_top	−0.99	9	192	2072	0.8
Pd111(O _{fcc}) ₇ (O _{tss}) ₉ /CO_top	−0.26	9	189	2090	0.7
Pd111(O _{fcc}) ₆ (O _{tss}) ₉ /CO_hcp	−1.02	9;9;9	214;214;215	1889	3.2
Pd111(O _{fcc}) ₆ (O _{tss}) ₉ /CO_top	−1.65	9	187	2083	0.9
Oxidized palladium nanoparticle					
Pd ₇₉ (O _{fcc}) ₆₂ /CO_top-cor	−0.49	6	200	2088	0.4
Pd ₇₉ (O _{fcc}) ₆₂ /CO_top-edg	0.04	7	203	2121	−0.1
Pd ₇₉ (O _{fcc}) ₅₉ /CO_top-cen	−1.48	9	188	2051	1.2
Pd ₇₉ (O _{fcc}) ₆₂ (O _{tss}) ₂₄ /CO_top-cor	−0.37	6	201	2095	0.2
Pd ₇₉ (O _{fcc}) ₆₂ (O _{tss}) ₂₄ /CO_top-edg	−0.63	7	194	2120	0.0
PdO(101) surface large unit cell					
PdO(101)/CO_top-3c	−1.49	3	189	2090	0.7
PdO(101)/CO_subs ^d	3.18	2;4;4	203;214;218	1540	7.2
PdO(101) surface small unit cell					
PdO(101)/CO_top-3c	−1.56	3	189	2084	0.8
PdO(101)/CO_subs ^e	3.13	2;4;4	201;214;218	1499	8.1
PdO(100) surface					
PdO(100)/CO_top-4c	−0.04	4	203	2131	−0.1

^a BE per CO adsorbate; ^b Coordination number of the Pd atom, on which the CO molecule is adsorbed with respect to the neighboring Pd atoms for the Pd₇₉ and Pd(111) models and with respect to the neighboring O atoms for the PdO(101) and PdO(100) models; ^c Elongation of the C-O bond upon adsorption with respect to the calculated bond length in the gas-phase CO of 114.2 pm; ^d O atom from the CO molecule interacts with two four-coordinated (surface and subsurface) Pd atoms, as the Pd–O distances are 224 and 229 pm, respectively; ^e O atom from the CO molecule interacts with two four-coordinated (surface and subsurface) Pd atoms, as the Pd–O distances are 221 and 228 pm, respectively.

On the oxidized Pd₇₉ NP model, CO can be adsorbed on low coordinated sites (corners and edges), even when all 62 surface fcc sites are occupied by O species (Figure 11). The BE is −0.49 eV on the most accessible corner sites, while on the edge sites, the BE value is ~ 0 eV, manifesting an unstable complex. The CO can be adsorbed at the terrace site if three neighboring O centers are removed from one of the (111) facets; at the Pd₇₉(O_{fcc})₅₉/CO_top-cen structure, the binding energy of an adsorbed CO molecule, −1.48 eV, is similar to the CO adsorption on the same terrace site of the pristine Pd₇₉ NP. We also considered CO adsorption on the Pd₇₉ NP model with all 62 surface fcc sites and 24 subsurface tss sites occupied by O centers. A comparison of the Pd₇₉(O_{fcc})₆₂/CO_top-cor and Pd₇₉(O_{fcc})₆₂(O_{tss})₂₄/CO_top-cor structures shows that the addition of subsurface O species slightly decreases the BE value from −0.49 to −0.37 eV. The highest BE value is found for the Pd₇₉(O_{fcc})₆₂(O_{tss})₂₄/CO_top-edg model, −0.63 eV, although the BE value in Pd₇₉(O_{fcc})₆₂/CO_top-edg is ~0 eV. Surprisingly, the geometries of both carbonyl complexes are the same—the Pd center is in a square planar configuration with respect to the neighboring O centers.

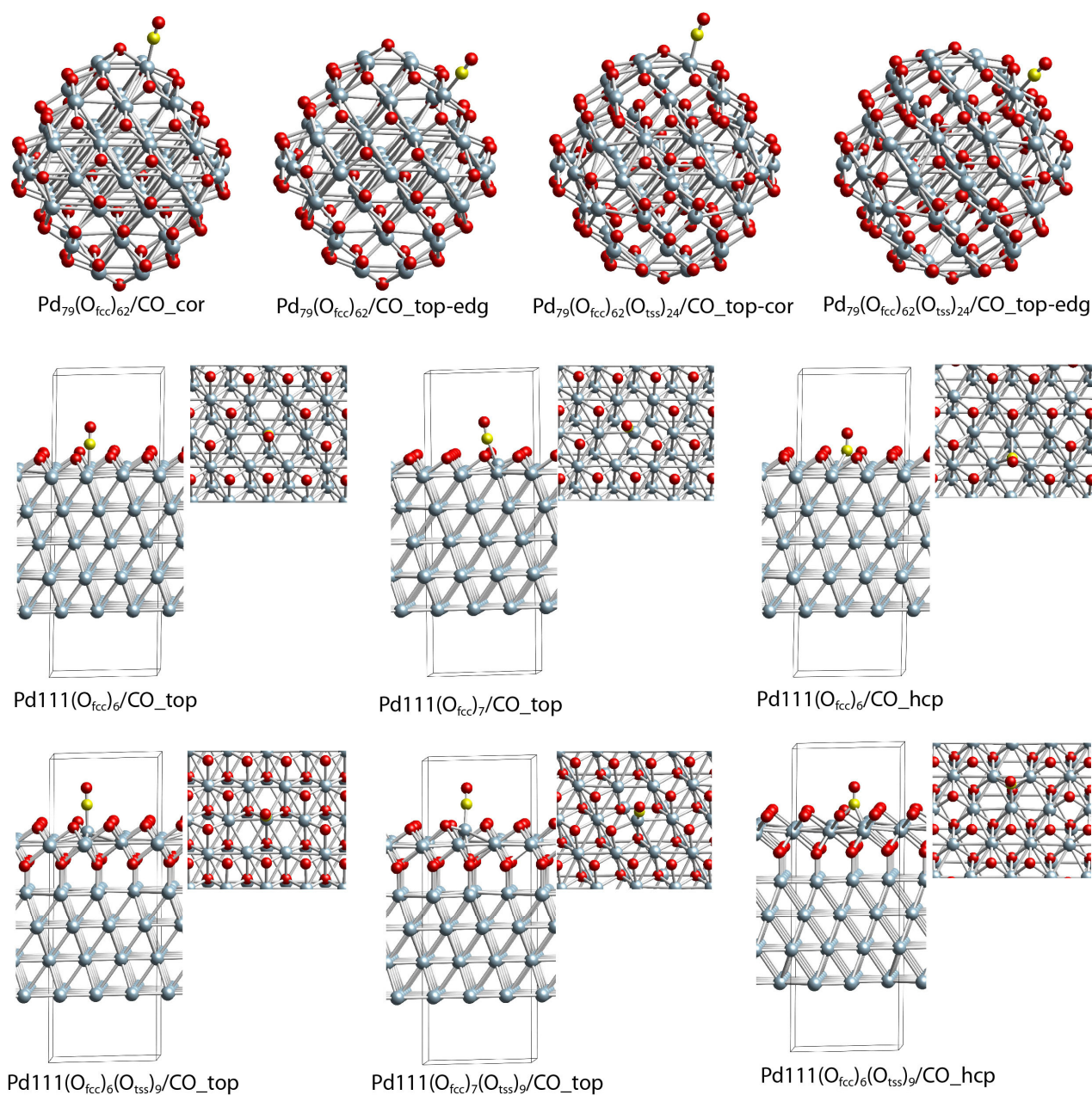


Figure 11. Adsorption complexes of CO on the O-containing Pd(111) slab and Pd₇₉ nanoparticle models. Color coding: light blue—Pd, red—O, and yellow—C. In the case of the Pd(111) surface also, the top view is shown as only the first two Pd layers are presented.

2.6. DFT Modeling Adsorption of CO Species on PdO(101) and PdO(100) Slab Models

The results obtained for both PdO(101) slab models are similar (Table 1, Figure 12); thus, only these obtained for the larger unit cell will be commented on in the text below. On the surface of the PdO(101) slab model, there are two types of Pd centers with coordination numbers three and four with respect to the closest O centers. We modeled CO adsorption on both surface positions, as the four-coordinated position is unstable, since the CO molecule migrates to a three-coordinated Pd center during geometry optimization. Indeed, in the most stable structure, PdO(101)/CO_{top-3c}, CO is adsorbed onto a three-coordinated surface Pd center, as the BE value, -1.49 eV, is similar to the corresponding value in the Pd₇₉(O_{fcc})₅₉/CO_{top-cen} structure (Table 2). We also optimized one more structure where CO is in the subsurface region, as the C atom interacts with two surface Pd centers and one subsurface Pd, while the O from the CO molecule interacts with one surface and

one subsurface Pd centers. However, this complex is very unstable, as the BE is strongly positive at 3.18 eV.

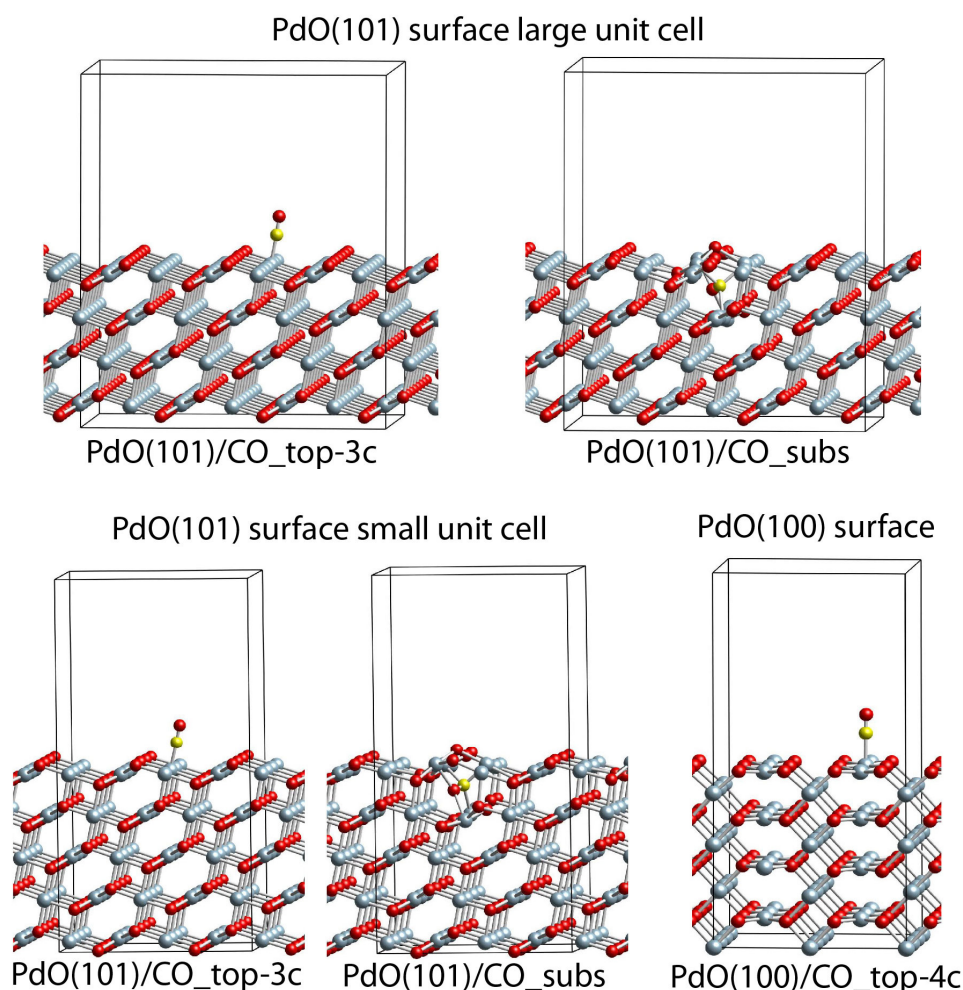


Figure 12. Adsorption complexes of CO on the PdO(101) and PdO(100) slab models. Color coding: light blue—Pd, red—O, and yellow—C.

One complex is found when CO is adsorbed onto the PdO(100) surface model, PdO(100)/CO_top-4c, where the CO interacts with a four-coordinated surface Pd center. The energy of CO in this case is only -0.04 eV.

2.7. Assignment of the Experimental C-O Vibrational Frequencies

In our previous study, we modeled CO adsorption at various surface sites of pristine Pd₇₉ NP [34]. Our results have shown that, when CO is at the top coordination (top-cen, top-edg, and top-cor), the calculated C-O vibrational frequencies, 2013 – 2023 cm^{-1} (presented also in Table 3), are systematically shifted to lower frequencies by ~ 60 cm^{-1} than the experimental bands. Similarly, the calculated C-O vibrational mode for CO adsorption at the top position of the Pd(111) surface slab model, 2036 cm^{-1} , is 51 cm^{-1} lower than the experimental band at 2087 cm^{-1} .

Table 3. Assignment of the C-O vibrational frequencies (in cm^{-1}) for CO adsorption on the Pd and PdO_x models and the experimental bands. The differences between the experimental and theoretical values ($\nu_{\text{exp}} - \nu_{\text{calc}}$) are given in parentheses.

Structures	CN ^a	ν_{calc}	ν_{exp}
<i>On-top slab</i> : Pd111/CO_top		2036	2087 (51)
<i>On-top terrace</i> : Pd ₇₉ /CO_top-cen ^b		2023	2087 (64)
<i>On-top edge</i> : Pd ₇₉ /CO_top-edg ^b		2015	2068 (53)
<i>On-top corner</i> : Pd ₇₉ /CO_top-cor ^b		2013	2068 (55)
Pd111(O _{fcc}) ₆ (O _{tss}) ₉ /CO_top	3	2083	2143 (60)
Pd111(O _{fcc}) ₇ /CO_top	3	2085	2143 (58)
Pd111(O _{fcc}) ₇ (O _{tss}) ₉ /CO_top	3	2090	2143 (53)
Pd ₇₉ (O _{fcc}) ₆₂ /CO_top-cor	3	2088	2143 (55)
PdO(101)/CO_top-3c	3	2090	2143 (53)
Pd ₇₉ (O _{fcc}) ₆₂ (O _{tss}) ₂₄ /CO_top-cor	3	2095	2143 (48)
Pd ₇₉ (O _{fcc}) ₆₂ /CO_top-edg	4	2121	2160 (39)
Pd ₇₉ (O _{fcc}) ₆₂ (O _{tss}) ₂₄ /CO_top-edg	4	2120	2160 (40)
PdO(100)/CO_top-4c	4	2131	2160 (29)

^a Coordination number of the Pd atom, on which the CO molecule is adsorbed with respect to the neighboring O atoms; ^b—data from Ref [29].

The calculated C-O vibrational frequencies in the Pd₇₉(O_{fcc})₆₂/CO_top-cor and Pd₇₉(O_{fcc})₆₂/CO_top-edg models, 2090 and 2121 cm^{-1} , are 77 and 106 cm^{-1} higher than the corresponding values in the O-free models, 2013 and 2015 cm^{-1} (Table 3). A similar increase of the C-O vibrational frequency from 2023 to 2051 cm^{-1} (Table 2) with the covering of the surface of the nanoparticle is also found for the CO adsorption at terrace top-cen sites, despite the fact that the three closest O centers around the Pd atom, which interacts with the CO molecule, are removed. These DFT results show that the increasing of the Pd oxidation state leads to the increase in the vibrational frequencies due to the increase of the σ -donation and electrostatic interaction, and the decrease of the π -back donation interaction between the palladium and CO ligand [35]. This is also in line with our experimental findings that CO bands of metallic Pd are at 2068 and 2087 cm^{-1} , while, for the palladium, the oxide systems are at 2143 and 2160 cm^{-1} . Interestingly, when CO is adsorbed on the PdO(101) and Pd(100) surfaces, the calculated C-O vibrational frequencies, 2090 and 2131 cm^{-1} , are similar to the corresponding values in the oxidized Pd(111) and Pd₇₉ models, where the Pd center to which CO is bound is with coordination numbers 3 and 4, respectively. Hence, our calculated C-O vibrational frequencies for the structures with CN = 3 at 2083–2095 cm^{-1} (Table 3) can rationalize the experimental band at 2143 cm^{-1} , while the band at 2160 cm^{-1} can be rationalized by the CO on the edge of the oxidized structures, as well as PdO(100)/CO_top-4c, where the calculated C-O vibrational frequencies are at 2120–2121 and 2131 cm^{-1} (Table 3). In these structures, the coordination number of Pd to which CO is bound is 4. These results are in agreement with the previous study of Martin et al. [36], where an IR band at 2132 cm^{-1} is assigned to CO adsorption on the Pd(101) surface.

3. Materials and Methods

3.1. Catalyst Preparation

Catalysts were prepared via the incipient wetness impregnation method using an aqueous solution of the Pd precursor ($\text{Pd}(\text{NH}_3)_4(\text{NO}_3)_2$) on Al_2O_3 (PURALOX TH 100/150, Sasol) and dried at 110 °C for 30 min. The cycles of impregnation–drying were repeated 3 times to obtain a homogenous distribution of Pd. The metal loading of the prepared catalysts was 5.5 wt%. The prepared catalysts were calcined at 500 °C under 20% O_2 in He (total flow rate = 1000 mL/min) for 2 h and hydrothermally aged at 850 °C for 10 h under 5.7% H_2O in the air. We chose 10 h of HTA at 850 °C to simulate the engine aging for 200 h in a vehicle. Pd/ Al_2O_3 -O_x was prepared via calcination (20% O_2 /He) at 500 °C for 2 h, and Pd/ Al_2O_3 -Red was prepared via reduction (10% H_2 /He) at 500 °C for 1 h.

3.2. CH₄ Oxidation Reaction Tests and CO Titration

CH₄ oxidation reaction tests were performed in a quartz flow reactor using 50 mg of the catalyst at 340 °C. Prior to the catalytic tests, the catalysts were calcined at 500 °C for 1 h in 20% O₂/He (flow rate = 60 mL/min). Reductive pretreatment was also conducted at 500 °C for 1 h in 10% H₂/He (flow rate = 60 mL/min). CH₄ oxidation activity was measured as a function of reaction time with a mixture of 1% CH₄ and 10% O₂ in He balance (total flow rate = 60 mL/min). The effluent gases were passed through a cold trap (dry ice) to remove the water produced during the reaction and then analyzed via gas chromatography (GC, Agilent 7820A) using a Carboxen-1010 column and a thermal conductivity detector. CO titration was also conducted by repeated pulse of 10% CO/He (sample loop = 1 mL) at 340 °C, following He purging. The effluent gases were passed through a methanator with 40% Ni/Al₂O₃ and analyzed using GC with flame ionization detector.

3.3. Catalyst Characterization

In situ DRIFTS experiments were performed using a Nicolet iS10 FTIR spectrometer equipped with a mercury cadmium telluride detector. The catalysts (13 mg) were loaded into a high-temperature reaction chamber (Harrick Scientific, New York, US) equipped with ZnSe windows, which were installed in a Praying Mantis diffuse reflectance accessory. Temperature ramping rate and gas flow rate were 10 °C/min and 60 mL/min, respectively. Loaded catalysts were pretreated using 10% O₂/He gas at 380 °C for 30 min and cooled to room temperature (RT) by flushing with He for 30 min. Thereafter, the chamber was heated again to 380 °C under 10% H₂/He, followed by He purging for 30 min and subsequent cooling under He flow. The background spectra were collected immediately after pretreatment. Afterward, CO adsorption using 0.2% CO/He was conducted. Each spectrum was obtained after He purging to remove the weakly bound CO and gas-phase CO. All spectra were collected using a resolution of 4 cm⁻¹, averaging 64 scans for every 50 s.

XRD patterns were obtained using a high-resolution X-ray diffractometer (Rigaku, Smartlab, Tokyo, Japan) with Cu K_α radiation ($\lambda = 1.54 \text{ \AA}$) in the step mode between 2 θ values of 10° and 80° with a step size of 0.02°/s. The tube voltage and current were 45 kV and 200 mA, respectively.

High-angle annular dark-field scanning transmission electron microscopy (HAADF-STEM) images were obtained using JEM2100F (JEOL) operated at an accelerating voltage of 200 kV.

3.4. Computational Details and Models

Periodic DFT calculations were performed using the plane-wave-based Vienna ab initio simulation package (VASP) [37,38]. We employed the exchange–correlation functional suggested by Perdew and Wang (PW91) [39] with an energy cutoff of 415 eV. For a description of the interaction between atomic cores and electrons, we used the projector augmented wave (PAW) method [40,41]. We sampled the Brillouin zone using the scheme of Monkhorst and Pack [42], as the mesh is 5 × 5 × 1 k points for the Pd(111) slab models, while, for the nanoparticle models, as well as the slab PdO(101) and PdO(100) models, only the Γ point was used (see below). The Methfessel–Paxton technique [43] was invoked to accelerate convergence with a width of 0.1 eV, as the final total energies were extrapolated to zero smearing.

The binding energies of the adsorbed CO molecules E_b were calculated as $E_b = -(E_{ad} + E_{sub} - E_{ad/sub})$, as E_{ad} is the total energy of the gas phase CO, E_{sub} is the total energy of the Pd substrate (either or not containing pre-ad(ab)sorbed species), and $E_{ad/sub}$ is the total energy of the substrate with all the adsorbates in the optimized geometry. Thus, negative E_b values indicate a favorable interaction, i.e., energy release during the adsorption process.

The shape of the employed Pd₇₉ nanoparticle (NP) model is a truncated octahedral. This structure exhibits eight (111) facets (each of them consisting of 12 surface Pd atoms) and six very small (100) facets (each of them consisting of four surface Pd atoms). The NP model is placed in a cubic cell with a lattice parameter of 2.0 nm.

We also employed an ideal Pd(111) surface model that was represented as five-layer slab repeated in a supercell geometry. The unit cell is (3×3) ; thus, the surface coverage of $1/9$ is achieved when one species is adsorbed into the unit cell. The ad/absorbates were bound to one side of the model and were allowed to relax during geometry optimizations together with the three adjacent (“upper”) layers of the substrate. The two “bottom” layers were kept fixed at the theoretical bulk-terminated geometry, where the Pd–Pd distance was 280 pm.

Other models that we employed were ideal PdO(101) and PdO(100) surfaces. In order to investigate the influence of the size of the unit cell in the former case, we considered two unit cells with a parallelepiped shape different in sizes. The larger one consisted of 144 Pd and 144 O atoms organized in a four-layer slab. The unit cell had dimensions: $a = 18.773$, $b = 18.620$, and $c = 21.800$ Å. The smaller one Pd₆₀O₆₀ was organized in a five-layer slab with dimensions: $a = 12.523$, $b = 9.288$, and $c = 24.110$ Å. The Pd(100) slab surface model was built from 48 Pd and 48 O atoms, with dimensions: $a = 9.288$, $b = 10.885$, and $c = 22.836$ Å, $\alpha = \beta = \gamma = 90^\circ$.

The available three-fold hollow Pd₃ adsorption sites for O and CO species on the Pd(111) slab and Pd₇₉ nanoparticle models were hcp (hexagonal close packed) or fcc (face-centered cubic) types (Figure 1). The center of these sites was below a Pd atom in the first and second subsurface layers, respectively. The subsurface sites beneath hcp and fcc—tetrahedral and octahedral sites, respectively—were denoted as tss and oss. Other adsorption positions available on the surfaces of both considered models were a top and bridge (denoted as br). They were located above a surface Pd and a Pd–Pd bond, respectively. In order to distinguish the surface and subsurface sites in Pd₇₉ NP, we added an additional tag for the following site locations: (cen)—at the center of a (111) facet, (edg)—at the edge between two (111) facets, and (cor)—at the corner between two (111) and one (100) facet (see Figure 1). The subsurface tetrahedral sites just below a surface Pd atom were denoted as tss’.

The activation energy barriers for O penetration from the surface to the subsurface region were derived by scanning the potential energy profile along the line that connects the local minima of the initial (surface) and final (subsurface) positions of the O species. Thus, estimations of the transition states (TSs) were searched in a pointwise fashion along the path connecting the adsorption and absorption configurations, where the height of the carbon atom, defined with respect to the most distant frozen metal layer, was fixed, whereas all other degrees of freedom were allowed to fully relax. The normal mode analysis verified that TSs have one imaginary mode that corresponds to O surface↔subsurface movement.

4. Conclusions

In this study, we investigated the intrinsic active sites of the Pd/Al₂O₃ catalyst for CH₄ oxidation, which interconverts between metallic Pd and PdO during the reaction. We used CO titration, in situ XRD, in situ DRIFTS, STEM, and periodic DFT calculations for the analysis. CO titration experiment and in situ XRD clearly showed that approximately 44% of PdO_x was formed from metallic Pd during the CH₄ oxidation reaction. In situ DRIFTS revealed that the topmost PdO_x surface is formed on the metallic Pd clusters during the reaction. STEM revealed the formation of the PdO layer on the metallic Pd cluster, and the DFT calculations also demonstrated that, in Pd nanoparticles, the migration of O from the surface to the subsurface region can be facilitated when the surface is O pre-covered, indicating the formation of surface PdO_x species. Based on all these results, we concluded that, during the CH₄ oxidation reaction, regardless of whether the initial state is Pd or PdO, the topmost surface is composed of PdO_x species, which is the catalytically relevant active phase. Furthermore, CH₄ oxidation activity profiles revealed that the surface PdO_x layer on the Pd core structure improves the catalytic durability of CH₄ oxidation, which is in agreement with the findings of previous studies. We believe our study will advance the understanding about the active sites of Pd-based catalysts and provide insights into the development of durable Pd-based catalysts for CH₄ oxidation.

Supplementary Materials: The following supporting information can be downloaded at: <https://www.mdpi.com/article/10.3390/molecules28041957/s1>, Figure S1: High-magnification STEM images of Pd/Al₂O₃-Ox (red) and PdAl₂O₃-Red (blue); Figure S2: In situ DRIFTS spectra of adsorbed CO on Pd/Al₂O₃-O_x (black) and Pd/Al₂O₃-Red after 3 min of CH₄ oxidation. DRIFTS spectra were recorded at 25 °C after He purging. The surface reconstruction from Pd to PdO immediately occurred within 3 min of the reaction. CH₄ oxidation condition—1% CH₄; 10% O₂ in He at 340 °C.

Author Contributions: Conceptualization, J.H.K., K.K. and H.A.A.; methodology, J.H.K., H.A.A. and G.N.V.; validation, J.H.K.; formal analysis, D.G.O., H.A.A. and G.N.V.; investigation, D.G.O., H.A.A., I.Z.K. and H.K.; resources, J.H.K.; data curation, J.H.K.; writing—original draft preparation, D.G.O.; writing—review and editing, J.H.K., D.G.O., H.A.A., I.Z.K., G.N.V. and H.K.; visualization, D.G.O. and I.Z.K.; supervision, J.H.K., K.K. and H.A.A.; project administration, J.H.K.; and funding acquisition, J.H.K. All authors have read and agreed to the published version of the manuscript.

Funding: We acknowledge the financial support from the National Research Foundation (NRF) (No. 2016R1A5A1009405 and 2017R1A2B4007310). H.A.A. is grateful for the support by the European Regional Development Fund and the Operational Program “Science and Education for Smart Growth” under contract UNITE No. BG05M2OP001-1.001-0004-C01 (2018–2023). I.Z.K. and G.N.V. acknowledge the support of the project EXTREME, funded by the Bulgarian Ministry of Education and Science, D01-76/30.03.2021, through the program “European Scientific Networks”. K.K. is grateful to the Quickstarter Initiative at Pacific Northwest National Laboratory under the Laboratory Directed Research and Development Program at PNNL, a multiprogram national laboratory operated by Battelle for the U.S. Department of Energy (DOE).

Institutional Review Board Statement: Not applicable.

Informed Consent Statement: Not applicable.

Data Availability Statement: Data are available by the authors.

Acknowledgments: H.A.A. and I.Z.K. acknowledge H.A.A. and I.Z.K. acknowledge computational resources provided by the e-infrastructure of the NCHDC—part of the Bulgarian National Roadmap on RIs, with the financial support by the Grant No D01-168/28.07.2022.

Conflicts of Interest: The authors declare no conflict of interest.

Sample Availability: Samples of the compounds are available from the authors.

References

1. Oh, D.G.; Lee, J.; Kim, E.; Jang, E.J.; Kim, J.M.; Kwak, J.H. Pd/SiO₂ as an active and durable CH₄ oxidation catalyst for vehicle applications. *J. Ind. Eng. Chem.* **2021**, *99*, 90–97. [[CrossRef](#)]
2. Stasinska, B.; Machocki, A.; Antoniuk, K.; Rotko, M.; Figueiredo, J.L.; Gonçalves, F. Importance of palladium dispersion in Pd/Al₂O₃ catalysts for complete oxidation of humid low-methane–air mixtures. *Catal. Today* **2008**, *137*, 329–334. [[CrossRef](#)]
3. Persson, K.; Pfeifferle, L.D.; Schwartz, W.; Ersson, A.; Järås, S.G. Stability of palladium-based catalysts during catalytic combustion of methane: The influence of water. *Appl. Catal. B Environ.* **2007**, *74*, 242–250. [[CrossRef](#)]
4. Kinnunen, N.M.; Hirvi, J.T.; Suvanto, M.; Pakkanen, T.A. Methane combustion activity of Pd–PdO_x–Pt/Al₂O₃ catalyst: The role of platinum promoter. *J. Mol. Catal. A Chem.* **2012**, *356*, 20–28. [[CrossRef](#)]
5. Castellazzi, P.; Groppi, G.; Forzatti, P.; Finocchio, E.; Busca, G. Activation process of Pd/Al₂O₃ catalysts for CH₄ combustion by reduction/oxidation cycles in CH₄-containing atmosphere. *J. Catal.* **2010**, *275*, 218–227. [[CrossRef](#)]
6. Mihai, O.; Smedler, G.; Nylén, U.; Olofsson, M.; Olsson, L. The effect of water on methane oxidation over Pd/Al₂O₃ under lean, stoichiometric and rich conditions. *Catal. Sci. Technol.* **2017**, *7*, 3084–3096. [[CrossRef](#)]
7. Lin, J.; Chen, X.; Zheng, Y.; Huang, F.; Xiao, Y.; Zheng, Y.; Jiang, L. Facile construction of ultrastable alumina anchored palladium catalysts via a designed one pot strategy for enhanced methane oxidation. *Catal. Sci. Technol.* **2020**, *10*, 4612–4623. [[CrossRef](#)]
8. Lin, J.; Zhao, L.; Zheng, Y.; Xiao, Y.; Yu, G.; Zheng, Y.; Chen, W.; Jiang, L. Facile Strategy to Extend Stability of Simple Component-Alumina-Supported Palladium Catalysts for Efficient Methane Combustion. *ACS Appl. Mater. Interfaces* **2020**, *12*, 56095–56107. [[CrossRef](#)]
9. Müller, C.A.; Maciejewski, M.; Koepfel, R.A.; Tschan, R.; Baiker, A. Role of Lattice Oxygen in the Combustion of Methane over PdO/ZrO₂: Combined Pulse TG/DTA and MS Study with ¹⁸O-Labeled Catalyst. *J. Phys. Chem.* **1996**, *100*, 20006–20014. [[CrossRef](#)]
10. Fujimoto, K.-i.; Ribeiro, F.H.; Avalos-Borja, M.; Iglesia, E. Structure and Reactivity of PdO_x/ZrO₂ Catalysts for Methane Oxidation at Low Temperatures. *J. Catal.* **1998**, *179*, 431–442. [[CrossRef](#)]

11. Au-Yeung, J.; Chen, K.; Bell, A.T.; Iglesia, E. Isotopic Studies of Methane Oxidation Pathways on PdO Catalysts. *J. Catal.* **1999**, *188*, 132–139. [[CrossRef](#)]
12. Jang, E.J.; Lee, J.; Oh, D.G.; Kwak, J.H. CH₄ Oxidation Activity in Pd and Pt–Pd Bimetallic Catalysts: Correlation with Surface PdOx Quantified from the DRIFTS Study. *ACS Catal.* **2021**, *11*, 5894–5905. [[CrossRef](#)]
13. Lyubovsky, M.; Pfefferle, L. Complete methane oxidation over Pd catalyst supported on α -alumina. Influence of temperature and oxygen pressure on the catalyst activity. *Catal. Today* **1999**, *47*, 29–44. [[CrossRef](#)]
14. Xu, J.; Ouyang, L.; Mao, W.; Yang, X.-J.; Xu, X.-C.; Su, J.-J.; Zhuang, T.-Z.; Li, H.; Han, Y.-F. Operando and Kinetic Study of Low-Temperature, Lean-Burn Methane Combustion over a Pd/ γ -Al₂O₃ Catalyst. *ACS Catal.* **2012**, *2*, 261–269. [[CrossRef](#)]
15. Hellman, A.; Resta, A.; Martin, N.M.; Gustafson, J.; Trincherio, A.; Carlsson, P.A.; Balmes, O.; Felici, R.; van Rijn, R.; Frenken, J.W.; et al. The Active Phase of Palladium during Methane Oxidation. *J. Phys. Chem. Lett.* **2012**, *3*, 678–682. [[CrossRef](#)] [[PubMed](#)]
16. Zorn, K.; Giorgio, S.; Halwax, E.; Henry, C.R.; Grönbeck, H.; Rupprechter, G. CO Oxidation on Technological Pd–Al₂O₃ Catalysts: Oxidation State and Activity. *J. Phys. Chem. C* **2011**, *115*, 1103–1111. [[CrossRef](#)]
17. Mehar, V.; Kim, M.; Shipilin, M.; Van den Bossche, M.; Gustafson, J.; Merte, L.R.; Hejral, U.; Grönbeck, H.; Lundgren, E.; Asthagiri, A.; et al. Understanding the Intrinsic Surface Reactivity of Single-Layer and Multilayer PdO(101) on Pd(100). *ACS Catal.* **2018**, *8*, 8553–8567. [[CrossRef](#)]
18. Datye, A.K.; Bravo, J.; Nelson, T.R.; Atanasova, P.; Lyubovsky, M.; Pfefferle, L. Catalyst microstructure and methane oxidation reactivity during the Pd \leftrightarrow PdO transformation on alumina supports. *Appl. Catal. A Gen.* **2000**, *198*, 179–196. [[CrossRef](#)]
19. Xiong, H.; Lester, K.; Ressler, T.; Schlögl, R.; Allard, L.F.; Datye, A.K. Metastable Pd \leftrightarrow PdO Structures During High Temperature Methane Oxidation. *Catal. Lett.* **2017**, *147*, 1095–1103. [[CrossRef](#)]
20. Farrauto, R.J.; Hobson, M.C.; Kennelly, T.; Waterman, E.M. Catalytic chemistry of supported palladium for combustion of methane. *Appl. Catal. A Gen.* **1992**, *81*, 227–237. [[CrossRef](#)]
21. Farrauto, R.J.; Lampert, J.K.; Hobson, M.C.; Waterman, E.M. Thermal decomposition and reformation of PdO catalysts; support effects. *Appl. Catal. B Environ.* **1995**, *6*, 263–270. [[CrossRef](#)]
22. Mouaddib, N.; Feumijantou, C.; Garbowski, E.; Primet, M. Catalytic oxidation of methane over palladium supported on alumina: Influence of the oxygen-to-methane ratio. *Appl. Catal. A-Gen.* **1992**, *87*, 129–144. [[CrossRef](#)]
23. Gelin, P.; Primet, M. Complete oxidation of methane at low temperature over noble metal based catalysts: A review. *Appl. Catal. B-Environ.* **2002**, *39*, 1–37. [[CrossRef](#)]
24. Eguchi, K.; Arai, H. Recent advances in high temperature catalytic combustion. *Catal. Today* **1996**, *29*, 379–386. [[CrossRef](#)]
25. Choudhary, T.V.; Banerjee, S.; Choudhary, V.R. Catalysts for combustion of methane and lower alkanes. *Appl. Catal. A-Gen.* **2002**, *234*, 1–23. [[CrossRef](#)]
26. Cullis, C.F.; Willatt, B.M. Oxidation of methane over supported precious metal catalysts. *J. Catal.* **1983**, *83*, 267–285. [[CrossRef](#)]
27. Eguchi, K.; Arai, H. Low temperature oxidation of methane over Pd-based catalysts—Effect of support oxide on the combustion activity. *Appl. Catal. A-Gen.* **2001**, *222*, 359–367. [[CrossRef](#)]
28. Ciuparu, D.; Lyubovsky, M.R.; Altman, E.; Pfefferle, L.D.; Datye, A. Catalytic combustion of methane over palladium-based catalysts. *Catal. Rev.* **2002**, *44*, 593–649. [[CrossRef](#)]
29. Lampert, J.K.; Kazi, M.S.; Farrauto, R.J. Palladium catalyst performance for methane emissions abatement from lean burn natural gas vehicles. *Appl. Catal. B-Environ.* **1997**, *14*, 211–223. [[CrossRef](#)]
30. Sekizawa, K.; Widjaja, H.; Maeda, S.; Ozawa, Y.; Eguchi, K. Low temperature oxidation of methane over Pd catalyst supported on metal oxides. *Catal. Today* **2000**, *59*, 69–74. [[CrossRef](#)]
31. Kovarik, L.; Jaegers, N.; Szanyi, J.; Derewinski, M.; Wang, Y.; Khivantsev, K. PdO self-assembly on zeolite SSZ-13 with rows of O3Al(IV)OH selectively incorporated in PdO(101) facets for moisture-resistant methane oxidation. *ChemRxiv* **2021**. [[CrossRef](#)]
32. Kan, H.H.; Colmyer, R.J.; Asthagiri, A.; Weaver, J.F. Adsorption of Water on a PdO(101) Thin Film: Evidence of an Adsorbed HO–H₂O Complex. *J. Phys. Chem. C* **2009**, *113*, 1495–1506. [[CrossRef](#)]
33. Lee, J.; Young Kim, M.; Hong Jeon, J.; Lee, D.H.; Rao, K.N.; Oh, D.G.; Jeong Jang, E.; Kim, E.; Na, S.C.; Han, H.S.; et al. Effect of Pt pre-sintering on the durability of PtPd/Al₂O₃ catalysts for CH₄ oxidation. *Appl. Catal. B Environ.* **2020**, *260*, 118098. [[CrossRef](#)]
34. Gun Oh, D.; Aleksandrov, H.A.; Kim, H.; Koleva, I.Z.; Khivantsev, K.; Vayssilov, G.N.; Hun Kwak, J. Key Role of a-Top CO on Terrace Sites of Metallic Pd Clusters for CO Oxidation. *Chem.–A Eur. J.* **2022**, *28*, e202200684. [[CrossRef](#)]
35. Hadjiivanov, K.I.; Vayssilov, G.N. Characterization of oxide surfaces and zeolites by carbon monoxide as an IR probe molecule. In *Advances in Catalysis*; Academic Press: Cambridge, MA, USA, 2002; Volume 47, pp. 307–511. [[CrossRef](#)]
36. Martin, N.M.; Van den Bossche, M.; Grönbeck, H.; Hakanoglu, C.; Zhang, F.; Li, T.; Gustafson, J.; Weaver, J.F.; Lundgren, E. CO Adsorption on Clean and Oxidized Pd(111). *J. Phys. Chem. C* **2014**, *118*, 1118–1128. [[CrossRef](#)]
37. Kresse, G.; Hafner, J. Ab initio molecular-dynamics simulation of the liquid-metal–amorphous-semiconductor transition in germanium. *Phys. Rev. B* **1994**, *49*, 14251–14269. [[CrossRef](#)]
38. Kresse, G.; Furthmüller, J. Efficiency of ab-initio total energy calculations for metals and semiconductors using a plane-wave basis set. *Comput. Mater. Sci.* **1996**, *6*, 15–50. [[CrossRef](#)]
39. Perdew, J.P.; Wang, Y. Accurate and simple analytic representation of the electron-gas correlation energy. *Phys. Rev. B* **1992**, *45*, 13244–13249. [[CrossRef](#)]
40. Blöchl, P.E. Projector augmented-wave method. *Phys. Rev. B* **1994**, *50*, 17953–17979. [[CrossRef](#)]

41. Kresse, G.; Joubert, D. From ultrasoft pseudopotentials to the projector augmented-wave method. *Phys. Rev. B* **1999**, *59*, 1758–1775. [[CrossRef](#)]
42. Monkhorst, H.J.; Pack, J.D. Special points for Brillouin-zone integrations. *Phys. Rev. B* **1976**, *13*, 5188–5192. [[CrossRef](#)]
43. Methfessel, M.; Paxton, A.T. High-precision sampling for Brillouin-zone integration in metals. *Phys. Rev. B* **1989**, *40*, 3616–3621. [[CrossRef](#)] [[PubMed](#)]

Disclaimer/Publisher’s Note: The statements, opinions and data contained in all publications are solely those of the individual author(s) and contributor(s) and not of MDPI and/or the editor(s). MDPI and/or the editor(s) disclaim responsibility for any injury to people or property resulting from any ideas, methods, instructions or products referred to in the content.